

Can Mineral Oil Slicks Be Distinguished From Newly Formed Sea Ice Using Synthetic Aperture Radar?

A. Malin Johansson , *Member, IEEE*, Martine M. Espeseth , *Member, IEEE*, Camilla Brekke , *Member, IEEE*, and Benjamin Holt , *Member, IEEE*

Abstract—In this feasibility study discriminating oil slicks and newly formed sea ice using synthetic aperture radar (SAR) imagery is investigated, using imagery from the L-band high-resolution uninhabited aerial vehicle synthetic aperture radar (UAVSAR) airborne and the satellite C-band RADARSAT-2 (RS-2) systems. To determine the separability of these two varying but similar appearing low backscatter ocean surfaces, multipolarization features are utilized from both SAR datasets. The discrimination is evaluated using the Kolmogorov–Smirnov separability test. All imagery was obtained during several sea ice campaigns in the Arctic Ocean and separate oil spill campaigns in Norway and the Gulf of Mexico, with each campaign collecting *in situ* observations. We observe that the polarization difference (VV–HH) reliably separates the mineral oil slicks and newly formed sea ice areas using UAVSAR images, due to the low noise floor and subsequent high signal-to-noise ratio (SNR) radiometric performance of the airborne system. The comparably higher noise floor and related lower SNR hampers the separability in the RS-2 images. Simulated noise floors were generated by adding white Gaussian noise to the UAVSAR data, which show that discrimination between the two low backscatter phenomena using multipolarization features is possible, provided that both datasets are still well above the noise floor. The pixel resolution has a limited effect on the separability. The results of this study provide an approach to distinguish oil slicks from newly formed sea ice, which might be of special interest should an oil spill occur within the marginal ice zone.

Index Terms—Oil slick, newly formed sea ice, synthetic aperture radar (SAR), polarimetry, uninhabited aerial vehicle synthetic aperture radar (UAVSAR), RADARSAT-2, signal-to-noise ratio (SNR), L-band, C-band.

I. INTRODUCTION

THE thinning of sea ice and the reduced sea ice cover in the Arctic [1] over the last decade has led to an increase in maritime traffic and petroleum-related activities, activities that

have associated potential risks of oil spills in this challenging environment [2]–[5]. There is a wide spread international concern of a potential spill in the Arctic environment, where detection of oil in ice-infested waters using synthetic aperture radar (SAR) is difficult during conditions of both new ice formation and ice concentrations greater than 40%, for smaller spills [6]. An oil spill within or near newly formed sea ice has not yet been known to occur nor captured on radar imagery. Therefore, in this feasibility study we examine the situation in radar imagery when sea ice appears most similar to an oil spill in an otherwise clean ocean, using both fully polarimetric (FP) and multifrequency data, in order to investigate the possibilities of discriminating between new ice formation and oil spills using uniform datasets. FP (HH/HV/VH/VV) satellite images have a small areal coverage and are not suitable for regular monitoring of the vast Arctic region. However, these images can be used to investigate whether various sea ice types and ocean conditions, including oil slicks and the similar-appearing sea ice can be discriminated using all three operationally available dual-polarimetric modes provided by presently operational satellite sensors such as Sentinel-1 (C-band), the RADARSAT Constellation Mission (C-band) and ALOS-2 (L-band).

We examine FP SAR images from spaceborne C-band RADARSAT-2 (RS-2) SAR images as well as airborne L-band SAR images acquired onboard the National Aeronautics and Space Administration (NASA) uninhabited aerial vehicle synthetic aperture radar (UAVSAR) sensor, to identify multipolarization features that can separate oil slicks from newly formed sea ice types over a range of incidence angles (IA). UAVSAR images were chosen due to the low instrument noise floor as well as the high resolution, and the RS-2 data based on the operationally used C-band frequency. The SAR data were acquired during sea ice field campaigns in the Arctic Ocean and oil spill field campaigns in the open ocean, i.e., the discrimination is tested between scenes containing either oil slicks or newly formed sea ice. *In situ* observations were also obtained during the respective campaigns which can be used for validation of both the sea ice and oil slicks properties. In Fig. 1, two photographs depicting the oil slicks from the oil-on-water (OOW) campaign in 2015 in the North Sea and in the Gulf of Mexico Mississippi Canyon 20 block (MC-20) are shown together with a photograph of newly formed sea ice observed during the Beaufort-Chukchi Sea 2015 campaign.

The article starts with Section II covering a review of related studies, followed by a description of the SAR data processing

Manuscript received March 31, 2020; revised June 12, 2020 and August 12, 2020; accepted August 13, 2020. Date of publication August 18, 2020; date of current version September 21, 2020. This work was supported in part by the Research Council of Norway (RCN) through “Oil spill and newly formed sea ice detection, characterization, and mapping in the Barents Sea using remote sensing by SAR” (OIBSAR) (RCN project 280616) and in part by the “Centre for Integrated Remote Sensing and Forecasting for Arctic Operations” (CIRFA) (RCN project 237906), and in part by the Jet Propulsion Laboratory, California Institute of Technology, under contract with the National Aeronautics and Space Administration. (Corresponding author: A. Malin Johansson.)

A. Malin Johansson, Martine M. Espeseth, and Camilla Brekke are with the Department of Physics and Technology, UiT The Arctic University of Norway, 9037 Tromsø, Norway (e-mail: malin.johansson@uit.no; martine.espeseth@uit.no; camilla.brekke@uit.no).

Benjamin Holt is with the Jet Propulsion Laboratory, California Institute of Technology, Pasadena, CA 91125 USA (e-mail: benjamin.m.holt@jpl.nasa.gov).

Digital Object Identifier 10.1109/JSTARS.2020.3017278

This work is licensed under a Creative Commons Attribution 4.0 License. For more information, see <https://creativecommons.org/licenses/by/4.0/>

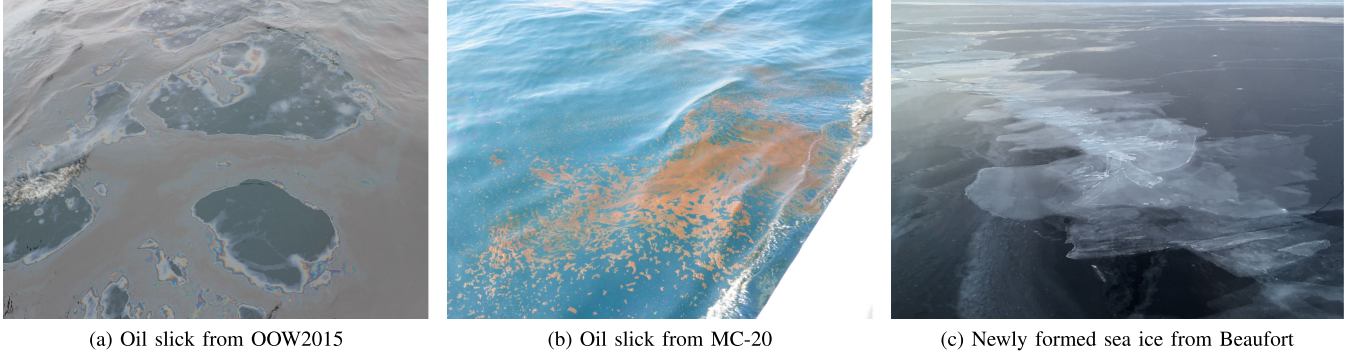


Fig. 1. (a) Closeup of an oil emulsion from the OOW2015 campaign on 10 June 2015, photo by Øyvind Breivik. (b) Oil slick observed in MC-20, photo by Benjamin Holt. (c) Newly formed sea ice from the Beaufort–Chukchi Sea campaign on 5 October 2015, photo by Benjamin Holt.

and the multipolarization features. In Section III the SAR data covering the OOW exercises and the sea ice campaigns are introduced. The methods used here are described in Section IV. Results and discussions are presented in Section V and finally Section VI concludes this article.

II. BACKGROUND AND POLARIMETRY

Low backscatter ocean signatures related to marine slicks and in young sea ice have been extensively studied for decades [7]–[10]. However, studies on discriminating oil slicks from newly formed sea ice using remote sensing instruments are sparse. Most studies, e.g., [11]–[14] focus on oil injection underneath the sea ice, investigations of the migration pattern of the oil up through newly formed sea ice, how oil is altered in cold temperatures and within sea ice and its subsequent impacts on the dielectric constant, and when the oil can be detected using various remote sensing instruments. One exception is [15] where they investigated utilizing FP SAR data, in this case the copolarization ratio and the phase difference for the two different mediums, based on a simple theoretical model of the dielectric constant.

With low backscatter we mean areas that relative to either a wind-roughened ocean surface or older/thicker sea ice, have a lower radar return, as well as being on the lower end of ocean-ice radar signatures. With respect to low backscatter for sea ice, the newly formed sea ice has been observed to be around 4–5 dB lower than, e.g., first-year ice in both C- and L-band SAR [16]. Similar results have been found in many other studies, primarily based on C-band SAR, e.g., [17], [18]. In [19] newly formed sea ice was reported to have backscatter values of -25 dB.

The damping of the surface waves from mineral oil slicks varies with type and thickness of oil (crude oil, water content in emulsified oils), age of the slick (weathering and emulsification), and of drift and mixing speed (wind and currents) see, e.g., [10], [20], [21]. The low backscatter may also be a result of a reduction of the complex dielectric constant (ϵ) [22]. The ϵ values for the mediums in L-band, are for clean water $58.26 - i41.48$ at -1.8°C and a salinity of 34.42 [23], for oil slick $2.3 - i0.01$ [24], [25] and for newly formed sea ice $4.23 - i0.12$ [26]. A study by [27] found that both the real and the imaginary part of the dielectric constant

were affected by oil within sea ice (a reduction in permittivity and reduced volume scattering), and were different from the uncontaminated sea ice (higher permittivity values and higher volume scattering). This finding indicates that this parameter may be useful to identify oil within sea ice.

Significant effort has gone toward establishing oil slick detection algorithms as well as developing discrimination tools relying on SAR data, e.g., [28]. In these studies, the shape of slicks is commonly used to separate the oil slicks from other low backscatter phenomena, but should an oil slick occur, e.g., at the ice margin, the sea ice edges may influence the spatial extent of the slick and, *feathering* as a descriptive feature may not occur. Out of the confirmed oil slicks in the HELCOM report [29] 76% were elongated, and thereby have a shape comparable to leads [30], an area where new ice regularly forms. Sea ice floes may also affect the shape of a slick and the oil may migrate underneath the sea ice. Therefore, the study here focuses on the backscatter and polarimetric parameter values and will not take into account the shape of the oil slicks, nor will it consider oil slicks under sea ice.

To establish multipolarization features that can be used for the separation between newly formed sea ice and open water, we use FP data that enables extraction of multipolarization features using the full scattering matrix \mathbf{S} as below

$$\mathbf{S} = \begin{bmatrix} S_{HH} & S_{VH} \\ S_{HV} & S_{VV} \end{bmatrix} = \begin{bmatrix} |S_{HH}|e^{i\phi_{HH}} & |S_{VH}|e^{i\phi_{VH}} \\ |S_{HV}|e^{i\phi_{HV}} & |S_{VV}|e^{i\phi_{VV}} \end{bmatrix}. \quad (1)$$

The first letter in the subscript refers to the transmitted polarization and the second to the received polarization. $|\cdot|$ and ϕ denote the amplitudes and the phases of the measured complex scattering coefficients. The images are first calibrated to sigma nought, and thereafter multilooked to reduce speckle.

A set of six different multipolarization features was selected for the separability analysis, listed in Table I. The selected multipolarization features emphasize different aspects of the backscatter information, such as the scattering processes and textural variation, and they have a proven suitability in discriminating oil slicks from surrounding open water (e.g., [22], [28], [31]) or in discriminating newly formed sea ice from surrounding thicker sea ice and open water (e.g., [16], [18], [32]). When

TABLE I
MULTIPOLARIZATION FEATURES USED IN THIS STUDY

Feature	Definition
Sigma nought backscatter	$\sigma_{HH}^0 = \langle S_{HH} ^2 \rangle$
Sigma nought backscatter	$\sigma_{VV}^0 = \langle S_{VV} ^2 \rangle$
Sigma nought backscatter	$\sigma_{HV}^0 = \langle S_{HV} ^2 \rangle$
Polarization difference	$PD = \langle S_{VV} ^2 \rangle - \langle S_{HH} ^2 \rangle$
Co-polarized ratio	$\gamma_{co} = \frac{\langle S_{VV} ^2 \rangle}{\langle S_{HH} ^2 \rangle}$
Cross-polarized ratio	$\gamma_{cr} = \frac{\langle S_{HV} ^2 \rangle}{\langle S_{HH} ^2 \rangle}$

The $\langle \cdot \rangle$ means that the data is averaged over a neighborhood of N pixels. We have assumed reciprocity $HV = VH$. PD is defined on a linear scale and may suppress nonpolarized scattering [38] and the other multipolarization features are defined on a log-scale.

analyzing SETHI airborne L-band SAR and UAVSAR data [28] found that out of 12 multipolarization features, σ_{HV} and σ_{VV} were the most suitable parameters for oil slick detection in open water, and the normalized radar cross section (NRCS) data are therefore included in the analysis. As available satellite data, such as from RS-2 and Sentinel-1 (S-1), provide the dual-polarization mode of HH/HV or VV/VH the cross-polarization ratio (γ_{cr}) is also investigated. For sea ice classification the copolarization ratio (γ_{co}) is a useful parameter for separating the thicker sea ice from thinner sea ice and open water areas, e.g., [16], [19], [32]. However, γ_{co} increases with IA for both the newly formed sea ice and mineral oil slicks [15], [18]. This IA dependence leads us to also include the polarization difference (PD) as it was shown to be less sensitive to IA variations compared to γ_{co} , to be less sensitive to additive noise [33]–[35] and less sensitive to the wind direction [34]. Initial studies using features derived from the covariance and coherency matrices were carried out, though these results were not as promising compared to the parameters included here and were therefore excluded from the study.

According to two-scale Bragg scattering models like tilted-Bragg model [36] or X-Bragg model [37], the multipolarization features above the line in Table I are dependent on both large and small scale surface roughness and below the line on large-scale roughness. All parameters are dependent on the IA and the dielectric constant.

III. EXPERIMENTAL SETUP AND DATA COLLECTION

In this study we use 11 multilooked complex (MLC) UAVSAR images, see Table II. The UAVSAR images were collected during the OOW2015 exercise in the North Sea [39], over a crude oil seep in the Gulf of Mexico in 2016, located at the MC-20 site [40], and during a sea ice campaign in Beaufort–Chukchi Seas in 2015 [41]. The images were chosen to cover a range of different IAs, spanning the entire range from 30° to 55° , though not all images contained dark features spanning the entire range. The upper restriction of 55° was set due to the increased influence from cross-talk at the higher IAs in spaceborne SAR systems, even though the UAVSAR

has a reliable calibration up to 58 degrees [42]. The MC-20 average slick size (approximately 14.9 km^2 [43]) and the newly formed sea ice areas were larger than those observed during the OOW2015 campaign, and therefore a larger number of images were required from the latter campaign to fully cover the same IA range. The UAVSAR images were not corrected for cross-talk [34].

In addition, we use 12 single-look complex (SLC) RS-2 images, separated into six different pairs. The oil slick RS-2 images were collected during four OOW exercises (2011–2013) and one was acquired near simultaneously with a UAVSAR image over MC-20. RS-2 images with overlapping IAs covering newly formed sea ice were selected from three different sea ice campaigns around Svalbard, in 2015 and 2019 respectively, for more details see [44] and the Research Council of Norway project Nansen Legacy website¹. The specifics for the UAVSAR and RS-2 data are presented in Table III.

A. Oil Slick Data

The OOW exercises are yearly oil spill response exercises conducted by the Norwegian Clean Seas Association for Operating Companies (NOFO). The exercises took place in the abandoned Frigg field in the North Sea ($59^\circ 59'N$, $2^\circ 27'E$), where controlled releases of mineral oil emulsions and plant oil into the open sea were conducted to test different recovery systems. The amount of oil released in each exercise was 20 m^3 (2011), 17 m^3 and 10 m^3 (2012), 50 m^3 (2013) and 43 m^3 and 35 m^3 (2015). Thickness estimates of 0.1–1.5 mm are given for the OOW 2011 [45]. The slicks were thin mineral oil emulsion films with an average water content of 58% – 69%. For further information about the specific mixtures and the exercises in 2011–2013, see, e.g., [45]–[47], and for the 2015 exercise see [39].

The other oil slick dataset was collected in 2016 over a persistent crude oil slick in MC-20. The crude oil slick undergoes emulsification upon surfacing and rapidly spreads as patchy areas of emulsified oil as well as most extensive sheen. Here four images from low to medium wind speed conditions are used [40]. *In situ* data indicate that the crude oil in MC-20 ranged in thickness from sheen to a thickness of 0.02–2 mm [40], [48].

B. Newly Formed Sea Ice Data

The UAVSAR sea ice data were collected during the Sea State and Boundary Layer field campaign which took place in the Beaufort–Chukchi Seas in October–November 2015 [41]. The thin ice thickness was calculated from skin temperatures measured by two KT-15 infrared thermometers, mounted on the ship and directed toward the sea surface at a distance of 25 m from the side of the ship. Each thermometer viewed an approximately 3-m wide area, with the two areas separated by 24 m. These ice thickness measurements have been validated with other related measurements and are accurate up to a thickness limit of 0.5 m [49]. The thickness measurements from October 6 are plotted on-top of a RS-2 ScanSAR Wide image in Fig. 2.

¹Online. [Available]: <https://arvenetternansen.com>

TABLE II
UAVSAR AND RS-2 IMAGE DATASETS

Datum (UTC)	Sensor and beam	# of images	IA (°)	Pair (#)	Age of spill (h)	Wind speed (m/s)	Air temp (°C)
OOW							
08 Jun 2011 05:59	RS-2 FQ28	1	46.1–47.3	5	18	1.6–3.3	11–16
08 Jun 2011 17:27	RS-2 FQ15	1	34.5–36.1	4	9	1.6–3.3	11–16
15 Jun 2012 06:20	RS-2 FQ11	1	30.3–32.0	3	14–22	4	8–9
15 Jun 2012 17:48	RS-2 FQ31	1	48.3–49.5	6	25–29	3	8–9
11 Jun 2013 17:19	RS-2 FQ9	1	28.1–29.8	2	1	5	9–11
09 Jun 2015 09:56 - 10:44	UAVSAR	1	29–40	-	3–4	5–7	9
10 Jun 2015 05:32 - 13:18	UAVSAR	3	31–67	-	17–25	9–12	9
MC-20							
15 Nov 2016 13:09 - 13:13	UAVSAR	1	41–52	-	-	5.9–6	22.3
17 Nov 2016 16:30 - 23:20	UAVSAR	2	31–50	-	-	3.9–5.4	23.4
17 Nov 2016 23:49	RS-2 FQW2	1	19.0–22.6	1	-	3.9–5.4	23.4
Beaufort							
06 Oct 2015 18:08 - 20:00	UAVSAR	4	26–64	-	-	4	-8.6
Svalbard							
26 Jan 2015 13:39	RS-2 FQ9	1	28.1–29.8	2	-	2	-31.4
20 Mar 2015 14:33	RS-2 FQ16	1	35.5–37.0	4	-	4	-26.2
30 Aug 2015 18:39	RS-2 FQ30	1	47.6–48.8	6	-	3	-3.4
01 Sep 2015 17:41	RS-2 FQ11	1	30.3–32.0	3	-	6	-3.3
06 Sep 2015 18:35	RS-2 FQ29	1	46.9–48.1	5	-	1	-0.5
02 Dec 2019 12:43	RS-2 FQ 2	1	19.7–21.6	1	-	7	-14.0

– indicates not applicable or not available information. For 17 November spatially and near temporally overlapping UAVSAR and RS-2 images were used over MC-20. RS-2 images are divided up into pairs (#), where each pair has similar IA, one containing oil slick and one newly formed sea ice. As MC-20 is a continuous seep no age of the spill is given. Temporally overlapping weather observations were measured onboard ships that participated in the OOW and sea ice exercises, though for 15 June 17:48 UTC 2012 wind speed observations from the closest platform is used. For MC-20 data from buoy 42020 from National Oceanic and Atmospheric Administration (NOAA) National Data Buoy Center are used. Differences in accuracy exist between the different campaigns, when possible one decimal is used.

TABLE III
SPECIFICS OF THE UAVSAR AND RS-2 DATA USED IN THIS STUDY. RANGE (RG) AND AZIMUTH (AZ) VALUES ARE GIVEN AS NOMINAL VALUES

Sensor	RS-2	UAVSAR
Operating mode	Spaceborne	Gulfstream-III aircraft
Frequency band	C (5.41 GHz)	L (1.26 GHz)
Acquisition mode	Fine Quad	PolSAR
Polarization mode	Full-polarization	Full-polarization
Resolution, m (Rg x Az)	5.2 x 7.6	1.5 x 0.8
Swath Width, km	25 x 25	22
Incidence angle (IA, °)	19–49	30–70
Noise Equivalent Sigma zero (NESZ), dB	-32.9 ±1.5	-52 to -35

The mean thin ice thickness during the day of the UAVSAR flights was 0.16 m and overall during the campaign the thinner sea ice thickness averaged 0.20 m. The air temperature ranged from -5°C to -10°C from October 4 through October 6, the date of the UAVSAR flight, with October 4 being the date when the ship entered the ice field. The water temperature remained below freezing -1.8°C throughout the campaign.

The RS-2 FP images were acquired during three different sea ice campaigns, Norwegian Young sea ICE cruise (N-ICE2015) [44], Fram Strait (FS) observatory cruise 2015, and the fourth Nansen Legacy campaign in 2019. The N-ICE2015 and Nansen Legacy campaigns were located north of Svalbard and FS15 close to the east coast of Greenland. During N-ICE2015 the newly formed sea ice observed in leads was in the form of nilas, young grey ice and young white ice [50]. During the three weeks of the FS15 campaign, sea ice had just started to form and newly formed sea ice with a thickness up to 4 cm was observed, primarily grease ice and nilas without frost flowers. During the

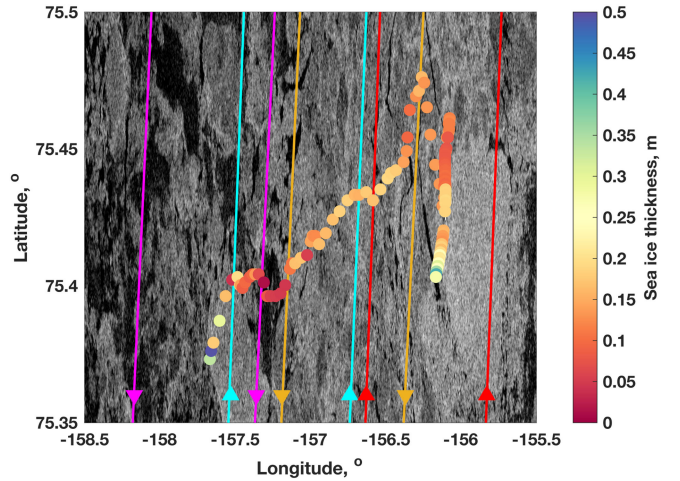


Fig. 2. Measurements of sea ice thickness were obtained from the Beaufort–Chukchi Seas 2015 campaign, utilizing downward-looking radiometers mounted on the ship as it traveled through the sea ice [49]. Sea ice thickness measurements (dots, m) are shown for October 6, which are overlaid on a RS-2 ScanSAR Wide HH-channel image taken on October 6, 2015 at 17:15 UTC. The greyscale on the RS-2 image ranges from -10 to -25 dB. The pairs of colored lines indicate the swath extent of the four separate UAVSAR acquisitions, and the arrows on the lines the flight direction.

Nansen Legacy campaign north of Svalbard in December 2019 new ice regularly formed during the freezing conditions.

IV. METHOD

UAVSAR and RS-2 images, presented in Table II, containing either mineral oil slicks or newly formed sea ice are used

to characterize the two types of low backscatter phenomena, with the aim to establish multipolarization parameters that can separate the two across a range of IAs. Six multipolarization features and their response to oil slicks and newly formed sea ice are investigated. A noise analysis is carried out to assess the SAR data quality and to identify potential limitations with the data for discrimination. The discrimination analysis is performed using the Kolmogorov–Smirnov (K–S) test [51] and finally, the importance of the signal-to-noise ratio (SNR) and the pixel resolution for the separability are assessed.

A. Feature Extraction

The multipolarization features are calculated using the equations outlined in Table I. The UAVSAR images were provided as multilook complex (MLC) data and were multilooked by 3×12 pixels, with an additional smoothing of 7×7 pixels performed to reduce radar speckle. The RS-2 SLC data were multilooked by 3×8 pixels.

Regions of interest (ROI) were manually identified and selected within each of the images to be representative of the mineral oil slicks and the newly formed sea ice areas, with example shown in Fig. 3(a) and (c). The ROIs for the MC-20 study area correspond to the areas with the highest damping ratios, shown in [52]. Also shown are the PD values for both areas [Fig. 3(b) and (d)]. In the ROI selection the edges of the respective low backscatter areas were avoided to reduce contamination from the surrounding open water and thicker sea ice. Structures such as ships and platforms were also avoided to mitigate effects from side-lobes that might otherwise smear the signal around the target. The UAVSAR images were collected during three separate campaigns and the low backscatter phenomenon covered a significant range of IAs. For this analysis, all pixels within the UAVSAR ROIs were separated into oil slick or newly formed sea ice pixels, and thereafter binned into five different IA ranges, where each range corresponds to 5° . The limited IA range covered by each RS-2 image prevented matching IA groupings. Instead, the six RS-2 image pairs, where each pair contained one oil slick and one newly formed sea ice image, were identified with overlapping IAs and all ROI pixels within each image were used for the analysis. The ROIs in the RS-2 images were equally sized for all pairs, though the shape was constrained by the slick or newly formed sea ice geometry and the 3×8 pixel multilooking. The same number of pixels was used for each pair, with >800 pixels for sets #1–4. A smaller number of pixels (>500) was used for sets #5–6 due to the smaller size of the oil slicks.

To quantify the heterogeneity within the different multipolarization features the coefficient of variation (\widehat{CV}) was calculated for all pixels within each IA range (UAVSAR) or image dataset (RS-2). \widehat{CV} is defined as

$$\widehat{CV} = \sigma_X / \mu_X \quad (2)$$

where σ is the standard deviation, μ is the mean value of X , the polarimetric feature. A low \widehat{CV} value indicates a largely homogeneous sample and a high value indicates large variations within the sample.

B. SAR Data Quality

The low radar return signal of the investigated mediums implies that the SNR needs to be considered when assessing the robustness of any multipolarization features. The NESZ is affected by many factors, including the SAR frequency, the incidence angle, and the azimuth resolution [53]. Here we observe a higher NESZ for the RS-2 images than for the UAVSAR images (Table III), controlled primarily by the two different altitudes of the sensors, as well as the increased NESZ with increasing frequency (see (5) in [53]). The higher NESZ for the RS-2 images and corresponding lower SNR has resulted in a lower separability between the ice/oil signatures and the clean ocean using the RS-2 data compared to the UAVSAR data. The effect of SNR on oil slick detection is extensively discussed in, e.g., [28], [33], and [54]. The level above the noise floor needed for the NRCS to safely contain a valid signal and be useful for polarimetric scattering analysis varies in the literature, e.g., at least 6 dB [22], 7–9 dB [34] up to 10 dB [19], [33]. When analyzing the NRCS values for the respective channels increments of 2 dB above the NESZ are therefore used, as this enables us to capture all three above mentioned ranges. The RS-2 NESZ values are calculated using the beam specified metadata information as well as the local IA [55]. The UAVSAR NESZ profile and further information is found in [42]. As the backscatter signals decrease with increasing IA, thereby reducing the SNR, the IA must also be considered in the analysis.

When comparing discrimination between the oil slicks and the newly formed sea ice and the potential influence of the SNR we define, for either of the two media, the difference (Δ) between the mean value, of the respective backscatter intensities and the NESZ as

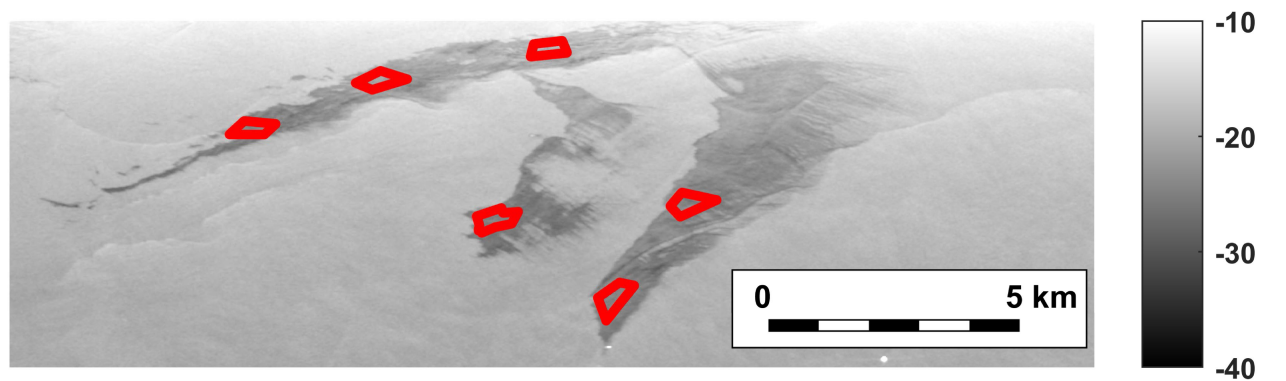
$$\Delta = \mu_X - NESZ. \quad (3)$$

C. Separability Analysis

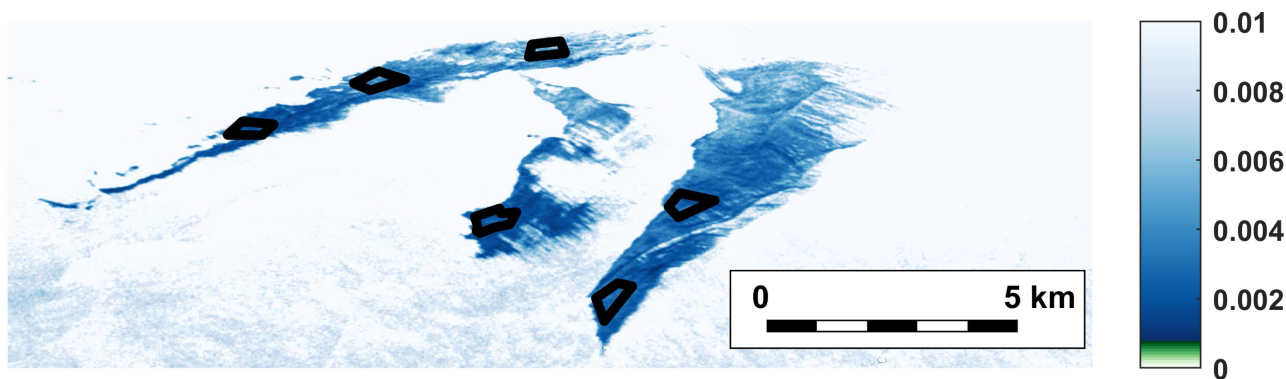
To investigate the separability between the mineral oil slicks and the newly formed sea ice we use the two sample K–S tests [51]. These tests are based on determining if two probability distributions are from the same distribution or not, by estimating the maximum difference between their cumulative distributions [56]. The test enables comparison between parameters that may not be normally distributed. The K–S test has values between 0 and 1 and here, similarly to [57] and [58], we define a K–S value above 0.7 to mean some separability, a value above 0.8 indicates reasonable separability and values above 0.9 represents good separability.

D. Effect of Additive Noise and Pixel Resolution

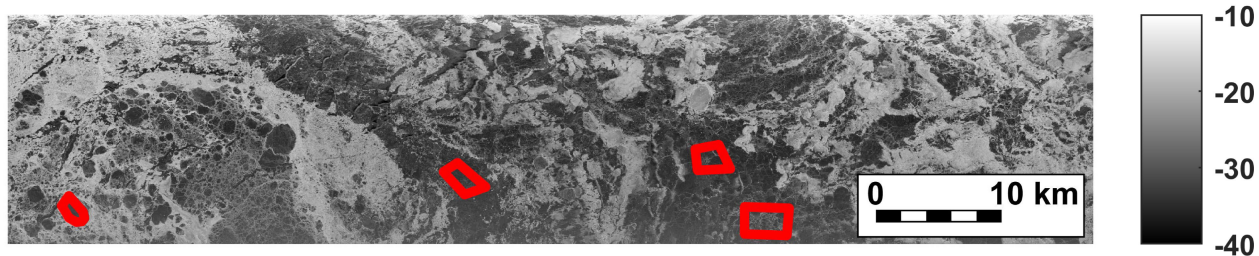
This step is only performed on the UAVSAR data, due to the sensors inherently good SNR and high pixel resolution. To test the influence of additive noise on the separability measure, we add simulated noise to the UAVSAR measurements, and compare the simulated noise to the true noise floors reported for RS-2 ScanSAR, S-1 Extra Wide (EW), and ALOS-2/PALSAR-2 Stripmap. The noise simulation is performed in the same manner as described in [33], where complex system noise is added to



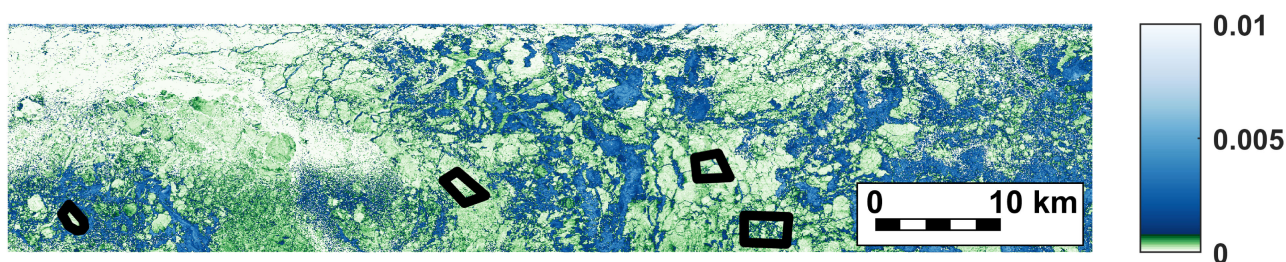
(a) UAVSAR intensity (VV), dB, image from the MC-20 area on November 17 2016 15:10 UTC.



(b) Polarization difference from the MC-20 area on November 17 2016 15:10 UTC.



(c) UAVSAR intensity (VV), dB, image from Beaufort Sea on October 6 2015 18:08 UTC.



Range
Azimuth

(d) Polarization difference from Beaufort Sea on October 6 2015 18:08 UTC.

Fig. 3. Intensity (VV) data in dB for UAVSAR images depicting (a) oil slicks in open water within the MC-20 area in the Gulf of Mexico and (c) newly formed sea ice among thicker sea ice in Beaufort Sea. The red areas indicate the ROIs used. The *PD* values for the respective UAVSAR images are shown in (b) for the oil slicks and in (d) for the newly formed sea ice. The same ROIs are here indicated with black polygons. Note that the colorbar is non-linear to enable the same color scale for both images.

the normalized radar backscatter coefficients. Expressed as

$$\mathbf{M} = \mathbf{S} + \mathbf{N} \quad (4)$$

where \mathbf{M} is the measured radar cross section, \mathbf{S} is the scattering matrix without noise (1), and $\mathbf{N} = [n_{HH}, n_{VH}, n_{HV}, n_{VV}]^T$ represents the complex additive noise. The additive noise is assumed to be complex Gaussian white noise with a mean around zero. From this procedure several new simulated noise floors or NESZ are generated. The separability estimates are thereafter carried out again using the range of new radar cross section values, starting from the polarimetric feature extraction stage.

The importance of the pixel spacing is investigated by varying the speckle filtering window size for the UAVSAR data. The original MLC UAVSAR images have been multilooked by 3×12 pixels, and here a running averaging filter was applied to the images, ranging from a 1×1 to a 20×20 pixel window size. The averaging will reduce the standard deviation of the values but not significantly affect the mean values. The new effective pixel spacings are also compared with the RS-2 ScanSAR, S-1 EW, and ALOS-2/PALSAR-2 Stripmap configurations. The original MLC UAVSAR images have a pixel spacing equivalent to the SLC RS-2 and ALOS-2 Fine Stripmap multipolarization data.

V. RESULTS AND DISCUSSION

In Fig. 3(a) and (b) we observe that there is a good oil–sea contrast in both σ_{VV} and PD for the UAVSAR data. This high oil–sea contrast for PD was also observed for three mineral oil emulsions (40%, 60%, and 80% volumetric oil fraction) in [34], and moreover, PD has a reduced dependence on IA for the oil slick compared to the open water. In Fig. 3(c) and (d), the newly formed sea ice can be detected in the σ_{VV} data though has a lower contrast to the surroundings in PD . Note that the PD values for the sea ice areas are lower than for the oil slick and open water areas, though for easier interpretation the same scale-bar is used in both sets of images.

A. Overall Observations

In Fig. 4(a) and (b), the mean σ_{HH} and σ_{VV} backscatter values for the respective ROIs and the dark slicks are plotted against mean PD , using the UAVSAR data. A good discrimination between the newly formed sea ice (blue dots) and the oil slicks (red triangles and magenta squares) is provided by PD . Moreover, the newly formed sea ice has overall lower backscatter, and lower PD values compared to the mineral oil slicks. Fig. 4(c) shows σ_{VV} plotted against γ_{co} , where a larger variability in the newly formed sea ice γ_{co} values compared to the PD values [Fig. 4(b)] can be observed. The corresponding results for the σ_{HH} and γ_{co} combination are not shown but provide a very similar outlook. The RS-2 data are shown in Fig. 4(d), where mean σ_{VV} is shown against mean PD values. A lower degree of separability can be observed compared to the UAVSAR data, though note that all ROI's from the different pairs are included and IA is not accounted for. For the RS-2 ice–oil pairs with the highest IAs the values approach the noise floor, and hence a reduced discrimination between the σ_{HH} and σ_{VV}

may be expected. Skrunes *et al.* 2018 [34] found that the PD values had a large decrease from 24° to 30° , though above this upper range the IA dependency was limited. From this it appears that PD versus σ_{VV} gives the overall cleanest separation for the UAVSAR data. Similar trends can be observed for the RS-2 data provided that the data are separated into distinct IA ranges.

There are many different environmental scenarios with respect to varying winds and currents, temperature, ice/oil, and water mixtures that need to be examined for the interdisciplinary topic of separating oil slicks from newly formed sea ice. Some of the scenarios are covered within this study, e.g., SAR images were acquired under low to medium wind conditions. For the RS-2 pairs care was taken to ensure similar wind conditions for the different pairs and also similar incidence angle, though small differences exist between the respective pairs. The air and water temperature variations are larger and may affect the dielectric constant values for the crude oil and oil–ice emulsions [27]. Excellent work has been carried out by, e.g., [11]–[14] to investigate the effect on oil spills underneath sea ice. Here we choose to focus on separability between oil slicks and newly formed sea ice, and assume to be located in the vicinity of each other within the marginal ice zone but not yet mixed in. This study is a feasibility study, since multipolarization SAR images covering both oil slicks and sea ice to the authors knowledge do not presently exist. Moreover, the work presented here requires that the newly formed sea ice and oil slicks have been detected and discriminated from their respective surroundings, and thereafter the separability between the two is assessed. For this we choose to include multipolarization parameters that [28] found to be suitable for oil spill detection and discrimination, and for sea ice discrimination [32]. Further investigations could be carried out using spaceborne L-band SAR data from, e.g., the ALOS-2/PALSAR-2 sensor, as it has both a low NESZ as well as high spatial resolution, though limited data are available overlapping oil spills.

B. Coefficient of Variation

The textural heterogeneity is quantified using \widehat{CV} . The correlation between sea ice thickness, IA, and the relative contributions of surface and volume scattering for different IAs, e.g., [18], [57], [59], means that we separate the \widehat{CV} values for the UAVSAR data into five IA ranges, presented in Table IV. The NRCS values for the dark features have low variability with IA, and γ_{co} , γ_{cr} , and PD have a higher dependency of IA. For all parameters the oil slick values are more homogeneous than the newly formed sea ice values for all IAs except the lowest one. The mineral oil slick in the MC-20 area had less variation with IA than the OOW2015 slicks. A potential reason for this is the higher wind speeds observed during the OOW2015 campaign, or the thinner slick may be more susceptible to breaking up. Skrunes *et al.* [34] observed the lowest \widehat{CV} values for PD for open water areas under OOW2015, and combined with the low IA dependency above 30° indicated that PD was one of the best operational multipolarization feature due to the stability under varying imaging geometry.

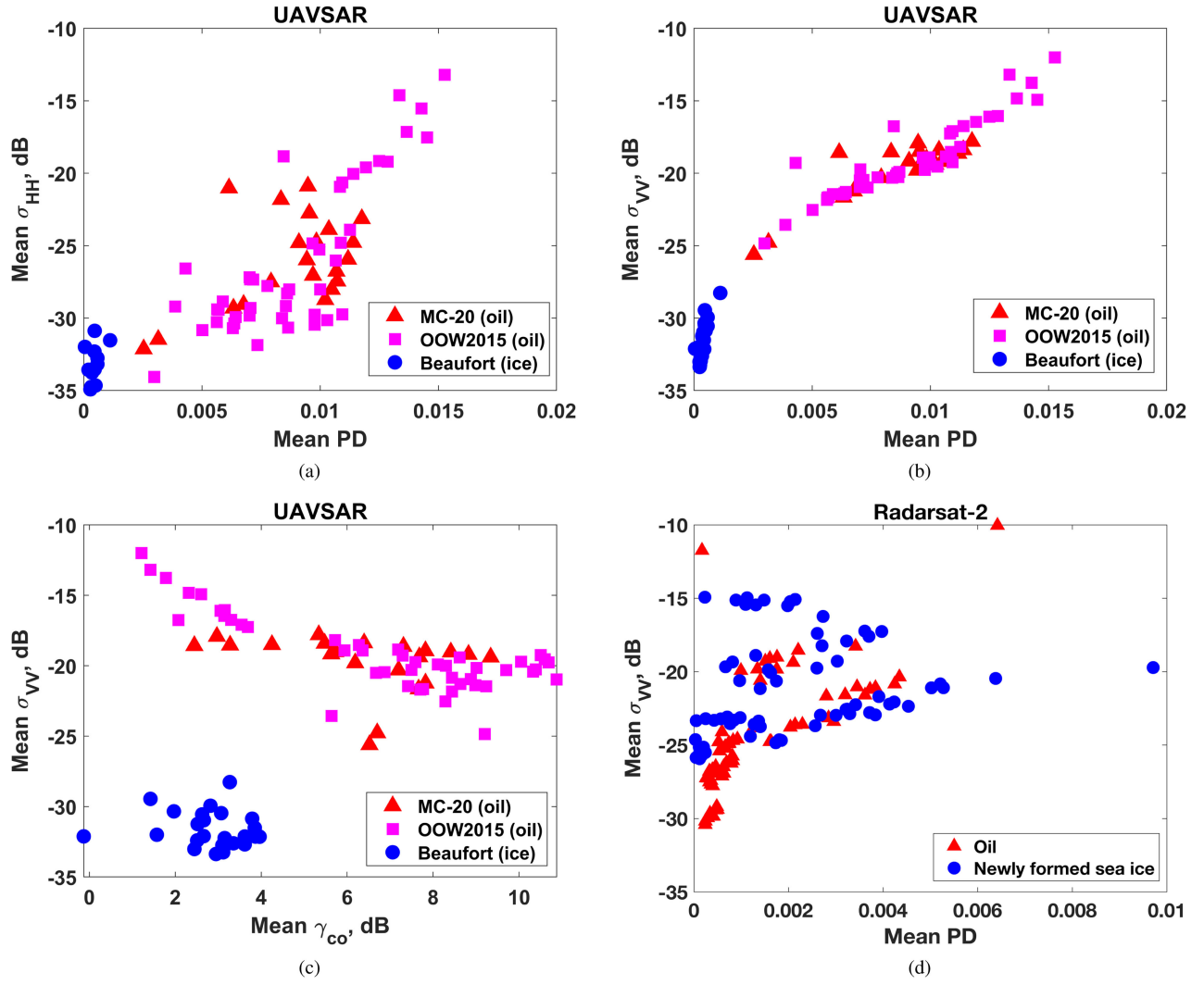


Fig. 4. UAVSAR mean PD is plotted against (a) mean σ_{HH} and (b) mean σ_{VV} , and in (c) mean σ_{VV} vs. mean γ_{co} . In (d) RS-2 mean PD against mean σ_{HH} . One marker indicates one individual ROIs, with no consideration for the IA bracket into which it falls.

TABLE IV
 \widehat{CV} VALUES FOR THE MULTIPOLARIZATION FEATURES ESTIMATED FROM THE UAVSAR DATA

IA		σ_{HH}	σ_{VV}	σ_{HV}	γ_{co}	γ_{cr}	PD
OOW2015	30°-35°	0.07	0.09	0.07	0.09	0.51	0.51
MC-20		0.15	0.14	0.06	0.11	0.20	0.27
Beaufort		0.09	0.10	0.04	0.10	0.41	0.54
OOW2015	35°-40°	0.08	0.11	0.07	0.16	0.37	0.47
MC-20		0.08	0.07	0.03	0.12	0.18	0.19
Beaufort		0.18	0.23	0.07	0.19	0.61	0.65
OOW2015	40°-45°	0.06	0.08	0.04	0.07	0.12	0.24
MC-20		0.06	0.05	0.02	0.09	0.15	0.20
Beaufort		0.17	0.27	0.07	0.29	0.72	1.73
OOW2015	45°-50°	0.09	0.13	0.08	0.16	0.27	0.41
MC-20		0.06	0.05	0.02	0.18	0.21	0.17
Beaufort		0.25	0.25	0.15	0.43	0.62	3.68
OOW2015	50°-55°	0.02	0.02	0.01	0.10	0.15	0.10
MC-20		0.06	0.05	0.02	0.16	0.24	0.22
Beaufort		0.22	0.27	0.12	0.45	0.56	1.70

The oil slick values are highlighted in light cyan and the newly formed sea ice in white. The data are split into IA ranges of 5° increments.

TABLE V
 \widehat{CV} VALUES FOR THE MULTIPOLARIZATION FEATURES ESTIMATED FROM THE RS-2 DATA

IA	Pair #	σ_{HH}	σ_{VV}	σ_{HV}	γ_{co}	γ_{cr}	PD
1	21°	0.16	0.17	0.04	8.07	0.08	6.73
		0.12	0.17	0.06	3.97	0.12	3.95
2	29°	0.10	0.10	0.05	1.68	0.17	1.73
		0.10	0.10	0.06	1.42	0.20	1.52
3	31°	0.08	0.08	0.04	1.53	0.29	1.62
		0.10	0.09	0.06	3.76	0.26	3.78
4	36°	0.07	0.08	0.04	1.48	0.41	1.81
		0.10	0.13	0.05	0.64	0.36	1.38
5	47°	0.04	0.05	0.04	1.02	1.85	1.13
		0.08	0.06	0.05	2.42	0.38	2.51
6	49°	0.05	0.07	0.03	0.51	0.47	0.74
		0.05	0.07	0.04	6.05	0.37	4.77

The oil slick values are highlighted in light cyan and the sea ice in white.

The \widehat{CV} values for the RS-2 data are shown in Table V. The low values for all NRCS values in pairs #5–6 are likely

a consequence of the low SNR. Notably higher values than for the other parameters were observed for PD . For pairs #3, 5 and 6 the $\widehat{CV}(PD)$ values for the newly formed sea ice are higher than for the oil slicks. Common for these three sea ice images is the recent drop in air and sea water temperature [60] and the measured sea ice thickness of 2–4 cm. Whereas for #2 the thickness was estimated to between 10–20 cm and #1 and 4 lacks thickness measurements. Studies by, e.g., [19], [61], [62], identified that when the sea ice thickness exceeds 2–4 cm, liquid brine forms at the sea surface, thereby changing the dielectric constant, and also changing the NRCS. The oil slicks studied in pairs #2 and 4 are the youngest slicks (<9 h), and in pair #1 is the large continuous release studied in MC-20. The relatively large variability may therefore be an effect of a more contained oil slick and a larger volume. The \widehat{CV} values here may have been affected by the low SNR and variability within the studied oil slicks and newly formed sea ice areas.

For the UAVSAR data we observe that \widehat{CV} of multipolarization features, e.g., PD , may be suitable for oil slick and newly formed sea ice discrimination, provided that the IA is $> 35^\circ$. Most operational SAR sensors provide data with IAs up to 47° – 50° , and hence such restrictions on the use of IAs are certainly possible. The two different UAVSAR oil slick datasets show similar results, this may be a result of the larger volumes of oil released within the MC-20 block, possibly resulting in a more coherent oil slick, or the different wind conditions under which the two slick areas were observed. The RS-2 data show higher \widehat{CV} values for PD when the measured sea ice thickness indicate values below 5 cm, though no consistent variability is observed.

C. Noise Analysis

Poor SNR may reduce the characterization ability and cause misinterpretations of the data [22], [28], [33]. To assess the data quality, the mean backscatter intensity values are compared to the NESZ at the same IA or range of IAs. In [19] and [33], a limit of 10 dB above the NESZ was determined to be at a level when polarimetric scattering properties of the target can be reliably assessed, [34] suggests using 7–9 dB, while [22] sets a value of 6 dB as being needed. In Fig. 5(a)–(c), the mean and one standard deviation backscatter values for the combined UAVSAR ROIs separated into 5° IA ranges are shown together with the NESZ values and 2dB increments above the NESZ, enabling comparison with the three suggested limits.

We observe that for the UAVSAR data the copolarization channels always meets the $>NESZ + 10$ dB criteria for both the mineral oil slicks and the newly formed sea ice areas. The HV-channel meets this criteria for all the OOW2015 images and for the IA bracket of 30° – 35° for the Beaufort images and for the 40° – 45° IA for the MC-20 images. The OOW2015 campaign has the highest wind speeds of the included data (see Table II), and this is likely a reason for the reduced effect of the sensor noise on this dataset. It may be possible to use the HV-channel for IAs up to 50° as it fulfills the criteria of $>NESZ + 6$ dB for all used datasets, though care must be taken in the interpretation of the results.

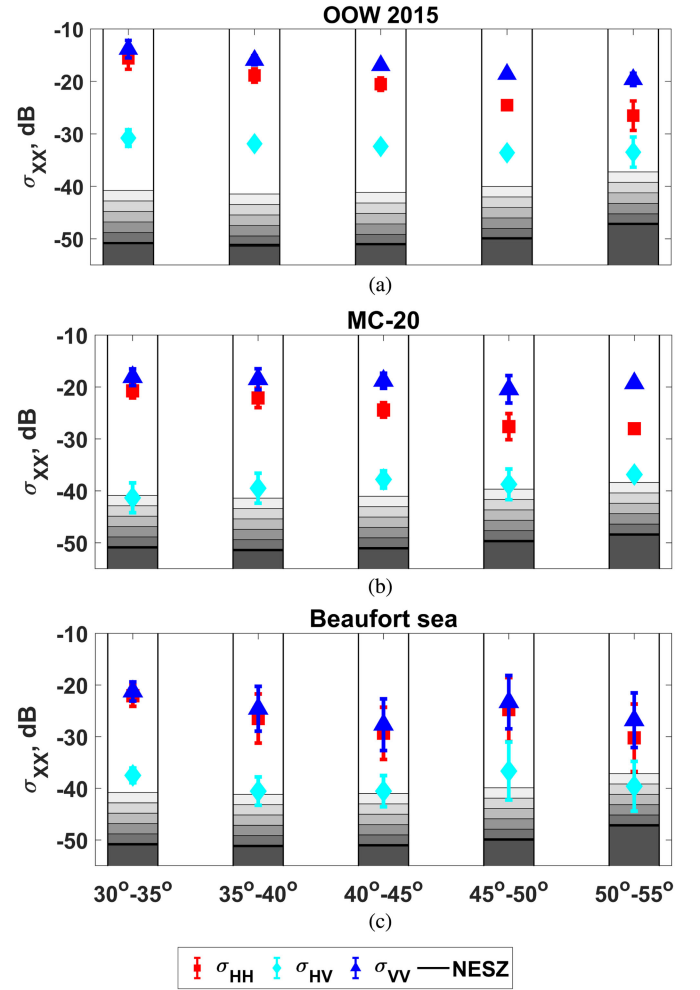


Fig. 5. UAVSAR backscatter $\sigma_{XX'}$ mean \pm std values plotted together with the NESZ for (a) OOW2015, (b) MC-20, and (c) Beaufort Sea. The NESZ values are illustrated using grey shading, where the darkest color represents values below the NESZ and white >10 dB above the NESZ. The shading is given in 2dB increments.

The noise analysis result for the RS-2 images are presented in Fig. 6. Note that for pair #1 the oil slick data was acquired in wide fine quad-polarimetric beam mode and the NESZ is therefore significantly higher than for the equivalent fine quad-polarimetric beam mode. For image pairs #1–2 both copolarized channels fulfil the $>NESZ + 10$ dB. When the mean plus one standard deviation fulfils $>NESZ + 10$ dB we define the SNR as good, when the values are below $NESZ + 10$ dB but above NESZ we define the SNR as moderate and when the values are below NESZ, as poor. The SNR values were good for the newly formed sea ice in pairs #1–3 and moderate in #4–6, and for the oil slick good in #1–2, moderate in pairs #3 and 6 and poor for pairs #4 and 5. For the cross-polarized channel the values were poor to moderate for all image pairs. The backscatter intensity values for the oil slicks in pair #6 are relatively high despite the high IA, this is possibly an effect of the age (25–29 h) of the observed oil slicks that may therefore have undergone more emulsification than the other slicks. In [35], they argue that the IA should, if possible, be kept below 35° to ensure a sufficient SNR

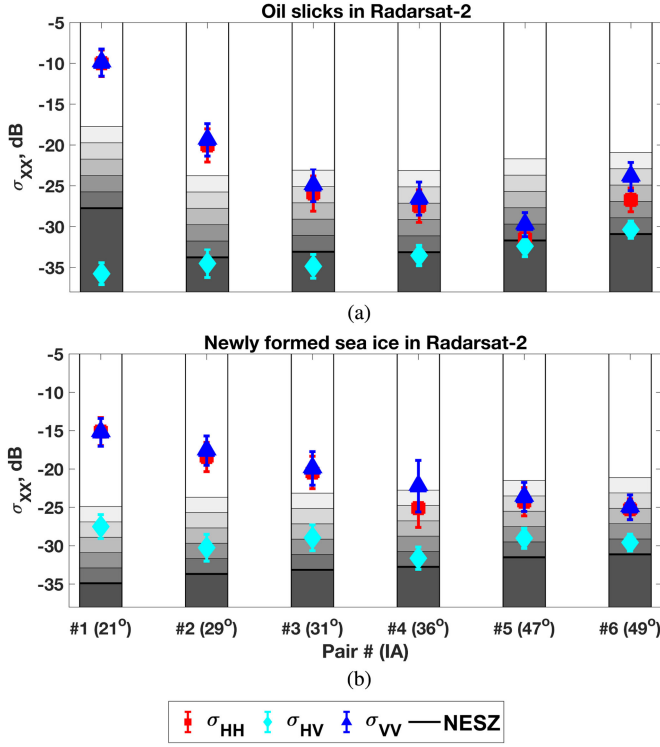


Fig. 6. RS-2 backscatter σ_{XX} mean \pm std values plotted together with the NESZ for (a) oil slicks and (b) newly formed sea ice. The NESZ values are illustrated using grey shading, where the darkest color represents values below the NESZ and white >10 dB above the NESZ. The shading is given in 2dB increments.

for newly formed sea ice areas, and the results here corroborate those findings.

From this section, we conclude that the UAVSAR data have sufficiently good SNR for the copolarization channels (due to the lower NESZ), though care must be taken when interpreting the result for the RS-2 images when the IA is $> 30^\circ$. For both the C- and the L-band data used here part of the cross-polarization data lie below the recommended limit of 10dB set by [19], and [33]. The low SNR for the cross-polarized data in RS-2 limits the usability of the σ_{HV} and γ_{cr} features. A detailed scattering analysis is not the objective of this study, and a lower SNR may be acceptable. However, the proximity to the noise floor and possible effects on the results should always be kept in mind when analyzing this type of data.

D. Kolmogorov–Smirnov Test: Discrimination of Oil and New Ice

To investigate separability between the mineral oil slicks and the newly formed sea ice, the K–S test for each IA range in the UAVSAR data is calculated (Table VI). For the MC-20 and Beaufort datasets the best separability was found using the PD and γ_{co} values. For both combinations of mineral oil slicks and newly formed sea ice, UAVSAR data PD provides good separability with only one value (0.77) below 0.9. It should be noted that the Beaufort and MC-20 data had similar wind speeds and that during the OOW2015 campaign the wind speeds were higher. The two highest IA bands (45° – 50° and 50° – 55°) for the

TABLE VI
K–S TEST BETWEEN THE MINERAL OIL SLICKS AND THE CORRESPONDING NEWLY FORMED SEA ICE FOR THE UAVSAR DATA

Beaufort and OOW2015						
IA	σ_{HH}	σ_{VV}	σ_{HV}	γ_{co}	γ_{cr}	PD
30° – 35°	0.84	0.92	0.90	0.67	0.16	1.00
35° – 40°	0.93	0.99	0.99	0.61	0.51	1.00
40° – 45°	0.90	0.97	0.95	0.80	0.45	1.00
45° – 50°	0.34	0.61	0.58	0.87	0.68	1.00
50° – 55°	0.63	0.74	0.79	0.74	0.35	0.97

Beaufort and MC-20						
IA	σ_{HH}	σ_{VV}	σ_{HV}	γ_{co}	γ_{cr}	PD
30° – 35°	0.35	0.66	0.72	0.99	0.90	0.99
35° – 40°	0.49	0.71	0.34	0.81	0.54	0.93
40° – 45°	0.58	0.85	0.73	0.99	0.58	0.94
45° – 50°	0.52	0.32	0.44	0.99	0.27	0.77
50° – 55°	0.62	0.82	0.75	1.00	0.32	1.00

We adopt the separability measures from [57], [58] where a K–S value above 0.7 means some separability (light green), a value above 0.8 indicates reasonable separability (mid green), and values above 0.9 have good separability (dark green).

TABLE VII
K–S TEST BETWEEN THE MINERAL OIL SLICKS AND THE CORRESPONDING NEWLY FORMED SEA ICE FOR THE RS-2 DATA

Pair #	IA	σ_{HH}	σ_{VV}	σ_{HV}	γ_{co}	γ_{cr}	PD
1	21°	0.71	0.73	0.91	0.21	0.96	0.21
2	29°	0.32	0.35	0.84	0.07	0.43	0.20
3	31°	0.81	0.79	0.96	0.15	0.10	0.32
4	36°	0.45	0.61	0.54	0.47	0.12	0.62
5	47°	0.99	0.93	0.81	0.29	0.72	0.32
6	49°	0.43	0.35	0.34	0.63	0.23	0.58

IA is the mean IA. We adopt the separability measures from [57], [58] where a K–S value above 0.7 mean some separability (light green), a value above 0.8 indicate reasonable separability (mid-green) and values above 0.9 have good separability (dark green).

Beaufort and MC-20 data are dominated by data with slightly higher wind speeds, approximately 6 m/s compared to 4 m/s. In these two cases we also observe lower K–S values for the single channel-based parameters. σ_{VV} and σ_{HV} overall provide some (>0.7) to good (>0.8) separability for the Beaufort and OOW2015 data. For both datasets σ_{HH} and γ_{cr} was found to be less suitable for discrimination between mineral oil slicks and newly formed sea ice, which is similar to findings in [28]. σ_{HH} had better overall separability in the OOW2015 and Beaufort dataset compared to the MC-20 and Beaufort dataset. The lower separability in γ_{cr} is important as most operational SAR sensors acquire wide-swath coverage images in the HH/HV mode in the Arctic Ocean context, and based on the findings here these images may not be suitable for discrimination between oil slicks and newly formed sea ice considering only the backscatter intensity values. For a discrimination using these type of images, such as S-1, inclusion of textural and spatial information is necessary.

The RS-2 data K–S distance are presented in Table VII. It can be observed that for some of the multipolarization features the K–S values are >0.7 for certain IAs, though no individual parameter was found to work for all datasets. The difference in separability compared with the UAVSAR data might be explained by the difference in SNR. In Fig. 7(a) and (b) the K–S values for the different image pairs are plotted against Δ (3) for the two different mediums, and in Fig. 7(c) the differences

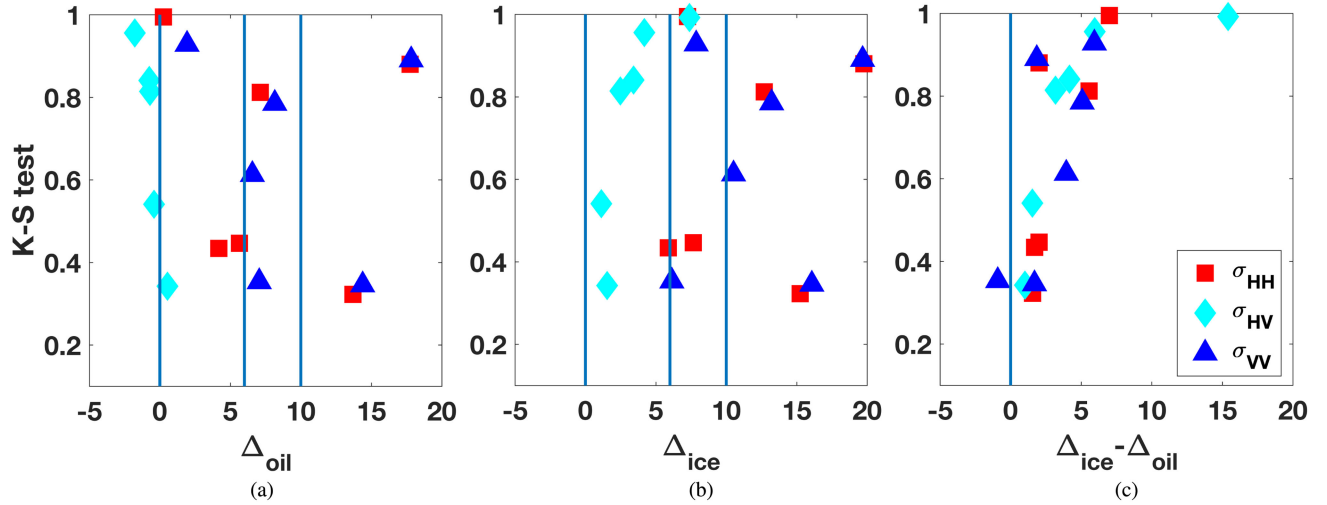


Fig. 7. RS-2 data K-S test values for σ_{HH} (red squares), σ_{HV} (cyan diamonds) and σ_{VV} (blue triangles) plotted versus Δ in dB for oil slicks (a), newly formed sea ice (b) and the difference in Δ for the newly formed sea ice and oil slicks (c). The vertical lines represent 0, 6, and 10 dB above the NESZ, respectively.

in Δ between the two different mediums are plotted against the K-S values. In the cases with the highest separability the Δ_{ice} values fulfils the criteria of at least NESZ + 6 dB. This may indicate a discrimination between a signal in the newly formed sea ice data and the higher noise component in the oil slick data. For the HV-data the Δ_{oil} values indicate that the oil slicks are close to or below the NESZ. Even though the Δ_{ice} values do not always have values of at least NESZ + 6 dB, they are higher than the Δ_{oil} values, again likely indicating a separation between a higher signal component due to a higher noise component.

PD can be used to reliably separate the investigated mineral oil slicks and newly formed sea ice using UAVSAR images, though for the RS-2 images the discrimination is hampered by the low SNR. PD has a high correlation with γ_{co} though the advantages with the reduced imaging geometry dependency of PD , the lower false alarm detection rate for oil slicks [28], the reduced dependency on additive noise [33], and the reduced influence of the wind to sensor direction [34] means that PD is preferable for discrimination between mineral oil slicks and newly formed sea ice for both datasets used here. However, the lower contrast between newly formed sea ice and thicker sea ice may limit the possibility of using PD for their discrimination, but γ_{co} has been proven to be useful for separating thinner sea ice from thicker sea ice [16], [18], [19], [32], [63]–[65]. Using a linear mixture model, the authors in [15] demonstrated that for L-band SAR the γ_{co} values for young ice are closer to the values for oil-ice emulsions than to open water values, and that newly formed sea ice have γ_{co} values higher than crude oil and oil-ice emulsions at -20°C . This was partially attributed to the higher dielectric constant for the newly formed sea ice. Using five complex permittivity mixture models [27] found that the temperature was very important for the dielectric constant values for crude oil and oil-ice emulsions and at -1.8°C the real permittivity values were similar to those for the newly formed sea ice. The dielectric loss factor was on the order one magnitude smaller than for the newly formed sea ice in [27] though one order of magnitude larger than modeled in [15].

Following the findings in this study, we suggest that a fully automatic detection and discrimination algorithm should first identify low σ_{HH} and σ_{VV} values, and thereafter do an assessment of the PD and γ_{co} values, similar to the discrimination presented in [32] where two thresholds were set for γ_{co} to separate the thin ice from open water (<2.8 dB) and from thicker sea ice types (>1.3 dB).

E. Additive Noise

The overall good separability using PD in the UAVSAR data meant that we select this parameter for further studies regarding the effect of additive noise to the NRCS values. In Fig. 8 the K-S test versus the simulated noise floors are shown for the Beaufort and MC-20 data. The results are comparable for the discrimination between the Beaufort and the OOW2015 data (not shown). The NESZ values for RS-2 multipolarization data, RS-2 dual-polarimetric data, and for S-1 EW are indicated with vertical lines, even though these sensors are C-band sensors, as they are commonly used for operational ocean surveillance. The NESZ values for the L-band ALOS-2/PALSAR-2 Stripmap high resolution mode are indicated for the HH-channel. When the simulated additive noise is approximately at the same level as the NESZ for S-1 EW the K-S discrimination is starting to be negatively affected by the additive noise. From this we conclude that significant noise levels can be added to the UAVSAR data before the discrimination between the newly formed sea ice and the oil slick is compromised. To ensure good separability and low false alarm rates in the detection of dark features the NESZ should if possible be below -24 dB. The backscatter values for the oil slicks and the newly formed sea ice will be affected by the frequency, and hence the sensitivity to the additive noise should be investigated for the different frequencies, particularly the commonly used C-band. Ideally, such an investigation should therefore be carried out using a multifrequency platform.

In addition to RS-2 and Sentinel-1, other current SAR satellites that are regularly used for ocean and sea ice surveillance

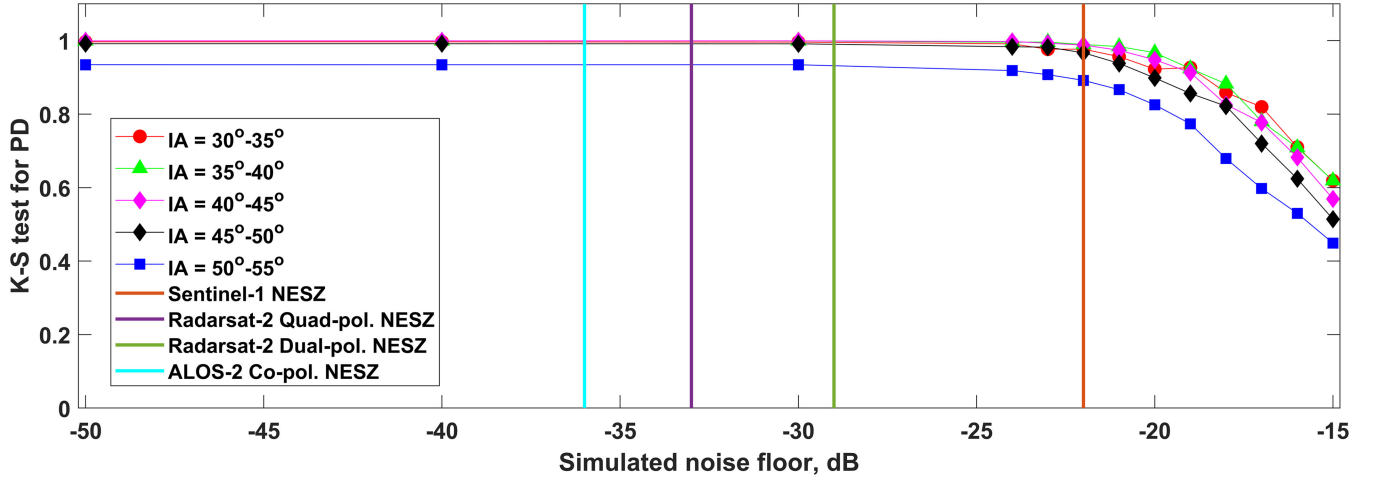


Fig. 8. K–S test for the Beaufort (ice) and MC-20 (oil) backscatter values with additive noise. The different colors represent different IA ranges. The x-axis shows the simulated noise floor levels that are derived from the UAVSAR measurements after Gaussian white noise is added to the measured signal. The original NESZ levels for the multipolarization and dual-polarimetric RS-2 modes, S-1 EW, and ALOS-2/PALSAR-2 Stripmap are indicated with vertical lines.

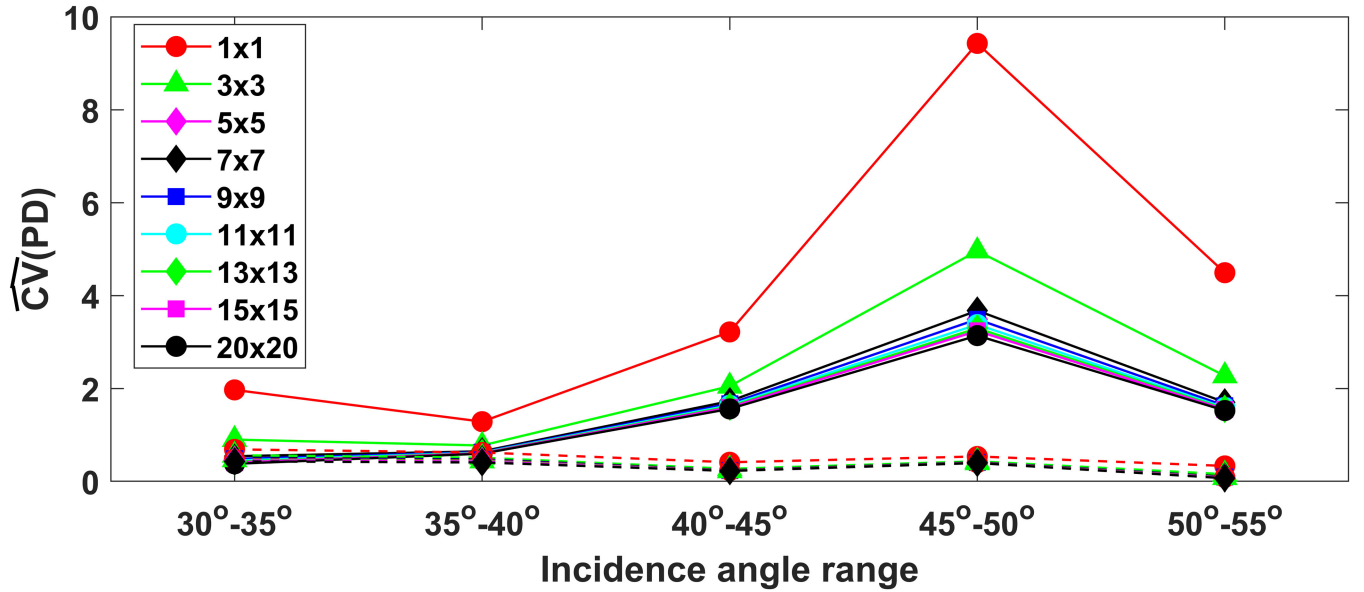


Fig. 9. \widehat{CV} values for PD for newly formed sea ice Beaufort (ice, solid lines) and MC-20 (oil, dashed lines) data with different sized averaging window. The different colored lines represent different smoothing window size. The x-axis show the different IA ranges.

include TerraSAR-X (NESZ = -17 dB [66]), ALOS-2 (NESZ for HH and VV = -36 dB, NESZ for HV = -46.0 dB [67]), and RADARSAT Constellation Mission (NESZ = -19 to -25 dB). The PALSAR-2 sensor onboard the ALOS-2 satellite has already been shown to have good potential for improved sea ice characteristics [68], [69]. Upcoming missions also include the NASA-ISRO SAR (NISAR) mission that will have sea ice coverage but also the capability to cover oil slicks, and offers both L- and S-band frequencies with NESZ of -25 dB [70].

Comparing the simulated additive noise level with the mean copolarization backscatter values, shown in Fig. 5, we observe that the mean backscatter values for the OOW2015 and MC-20 datasets are between -30 and -10 dB, whereas the Beaufort dataset has backscatter values between -18 and -33 dB. This seems to indicate that a good discrimination can be achieved as

long as one of the two investigated media has backscatter values above the noise floor, whereas when both media have values approaching the noise floor discrimination may be impaired. This is similar to the results for the RS-2 data shown in Fig. 7. The required backscatter values to separate low backscatter signatures including oil spills and newly formed sea ice (6 – 10 dB [19], [22], [33]) will vary in each of these systems, depending on the NESZ, available polarizations, and incidence angle examined.

F. Averaging Filter Size

The K–S test show a slight improvement for PD when the smoothing window size increases, though separability between 0.7 – 0.9 was found for all window sizes. The $\widehat{CV}(PD)$ values

in Fig. 9 indicate that the newly formed sea ice values remain similar once the window size is 5×5 or larger, whereas the oil slick values are stable regardless of window size. The pixel spacing corresponding to those of the RS-2 dual-polarimetric mode (6×6), S-1 EW mode (4×4), and ALOS-2 ScanSAR mode (5×5) and should, therefore, enable good separability provided sufficient SNR.

From this we conclude that for discrimination between oil slicks and newly formed sea ice, SNR is the most important parameter, and that for our dataset a pixel size similar to the one provided by S-1 EW did not hamper discrimination.

VI. CONCLUSION

We observe that PD can be used to reliably separate the investigated mineral oil slicks and newly formed sea ice using UAVSAR images, though low SNR hampers the separability in the RS-2 images used. The recently launched RADARSAT Constellation Mission (RCM) provides low resolution, high areal coverage acquisitions using both the copolarization channels as well as a dual polarization option, i.e., HH/HV, VV/VH, and HH/VV. Moreover, it has a compact polarimetry SAR mode where the 2nd component of the Stokes vector is similar to PD assuming reflection symmetry and reciprocity. The HH/VV ScanSAR option might be suitable for large-scale discrimination, and the compact polarimetric SAR mode is very promising for the detection and separation case of newly formed sea ice and oil slicks.

The high oil–sea contrast for PD in both the UAVSAR and RS-2 data indicates that it can be used both to detect oil slicks and separate them from the surroundings. However the lower newly formed sea ice and thicker sea ice contrast may limit the possibility of using PD both for detection and discrimination of oil slicks and newly formed sea ice. PD has a high correlation with γ_{co} though the advantages with the reduced imaging geometry dependency and the reduced dependency on additive noise means that PD is preferable for the discrimination. Simulated noise floors were generated by adding white Gaussian noise to the UAVSAR data, with the results indicating that discrimination between the two low backscatter phenomena was possible until the new noise floor reached -24 dB. The pixel resolution had limited effect on the separability.

ACKNOWLEDGMENT

The authors would like to thank NOFO for including our experiment in their exercise in 2015 and for providing ground truth data in 2011–2013 and 2015, scientists at the Norwegian Meteorological Institute for collecting metocean data, and KSAT for providing detection reports. Observations were provided for N-ICE2015 by the Norwegian Polar Institutes Centre for Ice, Climate and Ecosystems (ICE), FS15 by the Fram Strait Arctic Ocean Observatory (<http://www.npolar.no/framstrait>) and the Nansen Legacy cruise by the Nansen Legacy project (RCN project number 276730). The authors were grateful to all those who participated in the different fieldwork experiments.

The RS-2 image overlapping the MC-20 area was provided by MDA Geospatial Services (2016) and the RS-2 image covering

the sea ice and OOW exercises was provided by NSC/KSAT under the Norwegian–Canadian RADARSAT agreement 2011, 2012, 2013, and 2019. UAVSAR data can be downloaded from uavsar.jpl.nasa.gov or from the Alaska Satellite Facility (www.asf.alaska.edu). The publication charges for this article have been funded by a grant from the publication fund of UiT The Arctic University of Norway.

REFERENCES

- [1] J. Stroeve, T. Markus, W. Meier, and J. Miller, “The Arctic’s rapidly shrinking sea ice cover: A research synthesis,” *Climate Change*, vol. 110, pp. 1005–1027, 2012.
- [2] L. Pizzolato, S. Howell, C. Derksen, J. Dawson, and L. Copland, “Changing sea ice conditions and marine transportation activity in Canadian Arctic waters between 1990 and 2012,” *Climate Change*, vol. 123, pp. 161–173, 2014.
- [3] L. Pizzolato, S. Howell, J. Dawson, F. Laliberté, and L. Copland, “The influence of declining sea ice on shipping activity in the Canadian Arctic,” *Geophysical Res. Letters*, vol. 43, no. 23, pp. 12 146–12 154, 2016.
- [4] J. Wilkinson *et al.*, “Oil spill response capabilities and technologies for ice-covered Arctic marine waters: A review of recent developments and established practices,” *Ambio*, vol. 46, pp. 423–441, 2017.
- [5] L. C. Smith and S. R. Stephenson, “New trans-Arctic shipping route navigable by midcentury,” *PNAS*, vol. 110, no. 13, pp. E1191–E1195, 2013.
- [6] M. Babiker, K. Kloster, S. Sandven, and R. Hall, “The utilisation of satellite images for the oil in ice experiment in the Barents Sea,” SINTEF, Trondheim, Norway, Oil in Ice - JIP, Tech. Rep. 29, 44p, 2010.
- [7] H. Hühnerfuss, W. Alpers, and K. Richter, “Discrimination between crude-oil spills and monomolecular sea slicks by airborne radar and infrared radiometer-possibilities and limitations,” *Int. J. Remote Sens.*, vol. 7, no. 8, pp. 1001–1013, 1986.
- [8] W. Alpers and H. Hühnerfuss, “Radar signatures of oil films floating on the sea surface and the Marangoni effect,” *J. Geophysical Res. Atmospheres*, vol. 93, no. C4, pp. 3642–3648, 1988.
- [9] K. Singh, A. Gray, B. P. Hawkins, and R. O’Neil, “The influence of surface oil on C- and Ku-band ocean backscatter,” *IEEE Trans. Geosci. Remote Sens.*, vol. GE-24, no. 5, pp. 738–744, 1986.
- [10] M. Gade, W. Alpers, H. Hühnerfuss, V. R. Wismann, and P. A. Lange, “On the reduction of the radar backscatter by oceanic surface films: Scatterometer measurements and their theoretical interpretation,” *Remote Sens. Environ.*, vol. 66, pp. 52–70, 1998.
- [11] N. Firoozy *et al.*, “An electromagnetic detection case study on crude oil injection in a young sea ice environment,” *IEEE Trans. Geosci. Remote Sens.*, vol. 55, no. 8, pp. 4465–4475, 2017.
- [12] D. Desmond *et al.*, “Examining the physical processes of corn oil (medium crude oil surrogate) in sea ice and its resultant effect on complex permittivity and normalized radar cross-section,” *Marine Pollut. Bull.*, vol. 142, pp. 484–493, 2019.
- [13] M. Oggier, H. Eicken, J. Wilkinson, C. Petrich, and M. O’Sadnick, “Crude oil migration in sea-ice: Laboratory studies of constraints on oil mobilization and seasonal evolution,” *Cold Regional Sci. Technol.*, vol. 174, 2020, Art. no. 102924.
- [14] D. Saltymakova *et al.*, “Effect of dissolution, evaporation, and photooxidation on crude oil chemical composition, dielectric properties and its radar signature in the Arctic environment,” *Mar. Pollut. Bull.*, vol. 151, no. 110629, 2020.
- [15] C. Brekke, B. Holt, C. Jones, and S. Skrunes, “Discrimination of oil spills from newly formed sea ice by synthetic aperture radar,” *Remote Sens. Environ.*, vol. 145, pp. 1–14, 2014.
- [16] W. Dierking, “Mapping of different sea ice regimes using images from Sentinel-1 and ALOS synthetic aperture radar,” *IEEE Trans. Geoscience Remote Sens.*, vol. 48, no. 3, pp. 1045–1058, Mar. 2010.
- [17] R. Kwok, E. Rignot, B. Holt, and R. Onstott, “Identification of sea ice types in spaceborne synthetic aperture radar data,” *J. Geophysical Res.: Oceans*, vol. 97, no. C2, pp. 2391–2402, 1992.
- [18] R. G. Onstott, “SAR and scatterometer signatures of sea ice,” in *Microwave Sensing of Sea Ice*. Washington, DC, USA: Amer. Geophysical Union, 1992, pp. 73–104.
- [19] D. Isileifson, B. Hwang, D. G. Barber, R. K. Scharien, and L. Shafai, “C-Band polarimetric backscattering signatures of newly formed sea ice during fall freeze-up,” *IEEE Trans. Geosci. Remote Sens. Geoscience Remote Sens.*, vol. 48, no. 8, pp. 3256–3267, Aug. 2010.

- [20] W. Alpers and H. Hühnerfuss, "The damping of ocean waves by surface films: A new look at an old problem," *J. Geophysical Res.*, vol. 94, pp. 6251–6265, 1989.
- [21] I. Sergievskaya, S. Ermakov, T. Lazareva, and J. Guo, "Damping of surface waves due to crude oil/oil emulsion films on water," *Mar. Pollut. Bull.*, vol. 146, pp. 206–214, 2019.
- [22] B. Minchew, C. E. Jones, and B. Holt, "Polarimetric analysis of backscatter from the deepwater horizon oil spill using L-band synthetic aperture radar," *IEEE Trans. Geosci. Remote Sens.*, vol. 50, no. 10, pp. 3812–3830, Oct. 2012.
- [23] L. Klein and C. Swift, "An improved model for the dielectric constant of sea water in microwave frequencies," *IEEE J. Ocean. Eng.*, vol. 2, pp. 104–111, Jan. 1977.
- [24] K. Folgerø, "Bilinear calibration of coaxial transmission/reflection cells for permittivity measurement of low-loss liquids," *Meas. Sci. Technol.*, vol. 7, no. 9, pp. 1260–1269, 1996.
- [25] T. Friisø, Y. Schildberg, O. Rambeau, T. Tjomsland, H. Føredal, and J. Sjøblom, "Complex permittivity of crude oils and solutions of heavy crude oil fraction," *J. Dispersion Sci. Technol.*, vol. 19, no. 1, pp. 93–126, 1998.
- [26] N. Firoozy *et al.*, "A controlled experiment on oil release beneath thin sea ice and its electromagnetic detection," *IEEE Trans. Geoscience Remote Sens.*, vol. 56, no. 8, pp. 4406–4419, Aug. 2018.
- [27] T. Neusitzer *et al.*, "Examining the impact of a crude oil spill on the permittivity profile and normalized radar cross section of young sea ice," *IEEE Trans. Geosci. Remote Sens.*, vol. 56, no. 2, pp. 921–936, 2018.
- [28] S. Angelliaume *et al.*, "SAR imagery for detecting sea surface slicks: Performance assessment of polarization-dependent parameters," *IEEE Trans. Geosci. Remote Sens.*, vol. 56, no. 8, pp. 4237–4257, Aug. 2018.
- [29] HELCOM, "Joint final report on II audit of implementation of provisions of the convention on the protection of the marine environment of the Baltic Sea Area (Helsinki Convention) - Pollution from ships in the Baltic Sea," HELSINKI Commission, Riga, Latvia, Jan. 2005. [Online]. Available: <https://portal.helcom.fi/Archive/archive2/RESPONSE%205-2005%2010-1.pdf>
- [30] M. Konik and K. Bradtke, "Object-oriented approach to oil spill detection using ENVISAT ASAR images," *ISPRS J. Photogrammetry Remote Sens.*, vol. 118, no. 2016, pp. 37–52, 2016.
- [31] M. Migliaccio, A. Gambardella, and M. Tranfaglia, "SAR polarimetry to observe oil spills," *IEEE Trans. Geoscience Remote Sens.*, vol. 45, no. 2, pp. 506–511, 2007.
- [32] T. Geldsetzer and J. J. Yackel, "Sea ice type and open water discrimination using dual co-polarized C-band SAR," *Canadian J. Remote Sens.*, vol. 35, no. 1, pp. 73–84, 2009. [Online]. Available: <http://dx.doi.org/10.5589/m08-075>
- [33] M. Espeseth, C. Brekke, C. E. Jones, B. Holt, and A. Freeman, "The impact of system noise in polarimetric SAR imagery on oil spill observations," *IEEE Trans. Geosci. Remote Sens.*, vol. 58, no. 6, pp. 4194–4214, Jun. 2020.
- [34] S. Skrunes, C. Brekke, C. Jones, M. Espeseth, and B. Holt, "Effect of wind direction and incidence angle and polarimetric SAR observations of slicked and unslicked surfaces," *Remote Sens. Environ.*, vol. 213, pp. 73–91, 2018.
- [35] A. M. Johansson, C. Brekke, G. Spreen, and J. A. King, "X-, C-, and L-band SAR signatures of newly formed sea ice in Arctic leads during winter and spring," *Remote Sens. Environ.*, vol. 204, pp. 162–180, 2018.
- [36] G. Valenzuela, "Theories for the interaction of electromagnetic and oceanic waves—A review," *Boundary-Layer Meteorology*, vol. 12, no. 1–4, pp. 61–85, 1978.
- [37] I. Hajnsek, E. Pottier, and S. R. Cloude, "Inversion of surface parameters from polarimetric SAR," *IEEE Trans. Geosci. Remote Sens.*, vol. 41, no. 4, pp. 727–744, Apr. 2003.
- [38] V. Kudryavtsev, B. Chapron, A. Myasoedov, F. Collard, and J. Johannessen, "On dual co-polarized SAR measurements of the ocean surface," *IEEE Geosci. Remote Sens. Lett.*, vol. 10, no. 4, pp. 761–765, Jul. 2013.
- [39] I. H. Wasbotten, Oil budget and oil analysis, NOFOs, OPV2015, (in Norwegian), Akvaplan-niva AS, Troms, Norway, Tech. Rep. 7471-03, 2015.
- [40] C. Jones and B. Holt, "Experimental L-band Airborne SAR for oil spill response at sea and in coastal waters," *Sensors*, vol. 18, no. 2, 2018, Art. no. 641.
- [41] J. Thomson *et al.*, "Overview of the Arctic sea state and boundary layer physics program," *J. Geophysical Res.: Oceans*, vol. 123, pp. 8674–8687, 2018.
- [42] A. G. Fore *et al.*, "UAVSAR polarimetric calibration," *IEEE Trans. Geosci. Remote Sens.*, vol. 53, no. 6, pp. 3481–3491, Jun. 2015.
- [43] S. Sun, C. Hu, O. Garcia-Pineda, V. Kourafalou, M. Le Hénaff, and Y. Androulidakis, "Remote sensing assessment of oil spills near a damaged platform in the Gulf of Mexico," *Mar. Pollut. Bull.*, vol. 136, pp. 141–151, 2018.
- [44] M. A. Granskog, I. Fer, A. Rinke, and H. Steen, "Atmosphere-ice-ocean-ecosystem processes in a thinner Arctic sea ice regime: The Norwegian Young Sea ICE (N-ICE2015) expedition," *J. Geophysical Res.: Oceans*, vol. 123, no. 3, pp. 1586–1594, 2018.
- [45] S. Skrunes, C. Brekke, and T. Eltoft, "Characterization of marine surface slicks by Radarsat-2 multipolarization features," *IEEE Trans. Geosci. Remote Sens.*, vol. 52, no. 9, pp. 5302–5319, Sep. 2014.
- [46] S. Skrunes, C. Brekke, T. Eltoft, and V. Kudryavtsev, "Comparing near-coincident C- and X-band SAR acquisitions of marine oil spills," *IEEE Trans. Geosci. Remote Sens.*, vol. 53, no. 4, pp. 1958–1975, Apr. 2015.
- [47] S. Skrunes, C. Brekke, and A. Doulgeris, "Characterization of low-backscatter ocean features in dual-polarization SAR using log-cumulants," *IEEE Geosci. Remote Sens. Lett.*, vol. 12, no. 4, pp. 836–840, Apr. 2015.
- [48] O. Garcia-Pineda *et al.*, "Classification of oil spill by thicknesses using multiple remote sensors," *Remote Sens. Environ.*, vol. 236, 2020, Art. no. 111421.
- [49] P. Persson *et al.*, "Shipboard observations of meteorology and near-surface environment during autumn freezeup in the Beaufort/Chukchi seas," *J. Geophysical Res.: Oceans*, vol. 123, pp. 4930–4969, 2018.
- [50] M. A. Granskog *et al.*, "Snow contribution to first-year and second-year Arctic sea ice mass balance north of Svalbard," *J. Geophysical Res.: Oceans*, vol. 122, no. 3, pp. 2539–2549, 2017.
- [51] F. Massry, "The Kolmogorov-Smirnov test for goodness of fit," *J. Amer. Stat. Assoc.*, vol. 46, pp. 68–78, 1951.
- [52] M. M. Espeseth, C. E. Jones, B. Holt, C. Brekke, and S. Skrunes, "Oil-spill-response-oriented information products derived from a rapid-repeat time series of SAR images," *IEEE J. Sel. Topics Appl. Earth Observ. Remote Sens.*, vol. 13, pp. 3448–3461, 2020.
- [53] M. Younis, S. Huber, A. Patyuchenko, F. Bordoni, and G. Krieger, "Performance comparison of reflector- and planar-antenna based digital beam-forming sar," *Int. J. Antennas Propagation*, 2009, Art. no. 614931.
- [54] W. Alpers, B. Holt, and K. Zeng, "Oil spill detection by imaging radars: challenges and pitfalls," *Remote Sens. Environ.*, vol. 201, pp. 133–147, 2017.
- [55] RADARSAT-2 Product Description. Richmond, BC, Canada: Maxar Technologies, RN-SP-52-1238, Issue 1/13, Mar. 2016.
- [56] W. Press, S. Teukolsky, W. Vetterling, and B. Flannery, *Numerical recipes: The art of scientific computing*. New York, NY, USA: Cambridge Univ. Press, 2007.
- [57] T. Geldsetzer, M. Arkett, T. Zagon, F. Charbonneau, J. J. Yackel, and R. K. Scharien, "All-season compact-polarimetry C-band SAR observations of sea ice," *Can. J. Remote Sens.*, vol. 41, no. 5, pp. 485–504, 2015.
- [58] M. Daboor, B. Montpetit, S. Howell, and C. Haas, "Improving sea ice characterization in dry ice winter conditions using polarimetric parameters from C- and L-Band SAR Data," *Remote Sens.*, vol. 9, 2017, Art. no. 1270.
- [59] H. Wakabayashi, T. Matsuoka, K. Nakamura, and F. Nishio, "Polarimetric characteristics of sea ice in the Sea of Okhotsk observed by airborne L-band SAR," *IEEE Trans. Geosci. Remote Sens.*, vol. 42, no. 11, pp. 2412–2425, Nov. 2004.
- [60] M. Espeseth, S. Skrunes, C. Jones, C. Brekke, B. Holt, and A. Doulgeris, "Analysis of evolving oil spills in full-polarimetric and hybrid-polarity SAR," *IEEE Trans. Geosci. Remote Sens.*, vol. 55, no. 7, pp. 4190–4210, Jul. 2017.
- [61] D. Perovich and J. Richter-Menge, "Surface characteristics of lead ice," *J. Geophysical Res.*, vol. 99, no. C8, pp. 16 341–16 350, 1994.
- [62] D. Isleifson, R. Galley, N. Firoozy, J. Landy, and D. Barber, "Investigations into frost flower physical characteristics and the C-band scattering response," *Remote Sens.*, vol. 10, 2018, Art. no. 991.
- [63] M. Brath, S. Kern, and D. Stammer, "Sea ice classification during freeze-up conditions with multifrequency scatterometer data," *IEEE Trans. Geosci. Remote Sens.*, vol. 51, no. 6, pp. 3336–3353, Jun. 2013.
- [64] M. R. Drinkwater, R. Kwok, D. P. Winebrenner, and E. Rignot, "Multi-frequency polarimetric synthetic aperture radar observations of sea ice," *J. Geophysical Res.: Oceans*, vol. 96, no. C11, pp. 20 679–20 698, 1991.
- [65] D. P. Winebrenner, L. D. Farmer, and I. R. Joughin, "On the response of polarimetric synthetic aperture radar signatures at 24-cm wavelength to sea ice thickness in Arctic leads," *Radio Sci.*, vol. 30, no. 2, pp. 373–402, Mar./Apr. 1995.

- [66] T. Fritz and M. Einender, "TerraSAR-X ground segment basic product specification document," DLR, Cologne, Germany, Tech. Rep. TX-GS-DD-3302, 2013.
- [67] M. Shimada, M. Watanabe, T. Motohka, Y. Kankaku, and S. Suzuki, "Calibration and validation of PALSAR-2," *IEEE Int. Geosci. Remote Sens. Symp.*, 2015.
- [68] J. Karvonen, E. Rinne, H. Sallila, and M. Mäkynen, "On suitability of ALOS-2/PALSAR-2 dual-polarized SAR data for Arctic sea ice parameter estimation," *IEEE Trans. Geosci. Remote Sens.*, 2020, to be published, doi: [10.1109/TGRS.2020.2985696](https://doi.org/10.1109/TGRS.2020.2985696).
- [69] S. Singha, A. M. Johansson, N. Hughes, S. M. Munk Hvidegaard, and H. Skourup, "Arctic sea ice characterization using spaceborne fully polarimetric L-, C- and X-band SAR with validation by airborne measurements," *IEEE Trans. Geosci. Remote Sens.*, vol. 56, no. 7, pp. 3715–3734, Jul. 2018.
- [70] *NASA-ISRO SAR (NISAR) Mission Science Users' Handbook*. NASA Jet Propulsion Lab., Pasadena, CA, USA, Tech. Rep. 261, 2018.



A. Malin Johansson (Member, IEEE) received the M.Sc. degree in physical oceanography from Gothenburg University, Sweden, in 2005, and the Ph.D. degree in remote sensing from Stockholm University, Sweden, in 2012.

She is a Research Scientist with the Department of Physics and Technology, UiT The Arctic University of Norway, Troms, Norway, which she joined in 2014. She was a Postdoctoral Researcher with the Radar Remote Sensing group with the Department of Earth and Space Sciences, Chalmers University of

Technology, Gothenburg, Sweden. Her research interests include multisensor remote sensing of sea ice, oil spills, and harmful algae blooms.



Martine M. Espeseth (Member, IEEE) received the M.Sc. and Ph.D. degrees in remote sensing from the Department of Physics and Technology, UiT The Arctic University of Norway, Tromsø, Norway, in 2015 and 2019, respectively.

She is currently a Postdoc with the same department, with the Centre for Integrated Remote Sensing and Forecasting for Arctic Operations (CIRFA). From February to April 2016 and August to December 2018, she was a Visiting Ph.D. student with the Jet

Propulsion Laboratory, California Institute of Technology, Pasadena, CA, USA. Her current research interests include remote sensing of polarimetric SAR and with a focus on compact polarimetry within both marine oil pollution and sea ice applications.



thetic aperture radar and ocean color remote sensing for Arctic and marine applications.

Camilla Brekke (Member, IEEE) received the Cand. Mag., Cand. Scient., and Ph.D. degrees from the Department of Informatics, University of Oslo, Oslo, Norway, in 1998, 2001, and 2008, respectively.

She is currently the Vice-Dean Research with the Faculty of Science and Technology, the Deputy Centre Leader with the Centre for Integrated Remote Sensing and Forecasting for Arctic Operations and full Professor at Department of Physics and Technology, UiT The Arctic University of Norway, Tromsø, Norway. Her current research interests include syn-



Benjamin Holt (Member, IEEE) received the B.A. degree in human biology from Stanford University, Stanford, CA, USA, in 1972, and the M.S. degree in physical oceanography from the University of Southern California, Los Angeles, CA, USA, in 1988.

He is a Research Scientist with the Ocean Circulation group within the Earth Science Section at the Jet Propulsion Laboratory, California Institute of Technology, Pasadena, CA, USA, since 1978. His research interests include using multisensor remote sensing data to examine the geophysical state of polar sea

ice and snow, coastal oceanography and circulation, and the detection of marine pollutants. In addition, he is also involved with new instrument development and techniques for microwave measurement of sea ice thickness.